Optics Letters

Tunable strong circular dichroism at large-angle oblique incidence via plasmonic bound states in the continuum

Yi Zhong, Zhuo Wang,* Yixiong Wang, and Sheng Lan

Guangdong Provincial Key Laboratory of Nanophotonic Functional Materials and Devices, School of Optoelectronic Science and Engineering, South China Normal University, Guangzhou 510006, China
**zhuowang@m.scnu.edu.cn*

Received 1 July 2025; revised 17 August 2025; accepted 20 August 2025; posted 21 August 2025; published 12 September 2025

Plasmonic metasurfaces with chiral responses have attracted significant research interest because of their capacity to manipulate light spin. However, existing research indicates that strong circular dichroism (CD) responses are typically limited to normal incidence or small-angle oblique incidence (≤60°), hindering applications under highly oblique illumination. To overcome this, we propose a plasmonic metasurface featuring cross-shaped metal-insulator-metal unit cells for creating strong extrinsic chiral quasi-bound states in the continuum. Simulations demonstrate near-perfect absorption around 75° oblique incidence, achieving a high quality factor (~76) and strong reflected CD (~0.84). Crucially, the chiral response is reversible simply by adjusting the azimuth angle of incidence, facilitating dynamic CD modulation in a wide range from −0.82 to 0.84. This work presents a scheme for constructing and manipulating intense CD responses under large-angle oblique incidence, advancing the design of high-performance systems for on-chip spin selection and chiral biosensing.

https://doi.org/10.1364/OL.572000

Bound states in the continuum (BICs) are nonradiative states that overlap with the radiation continuum. This concept was first proposed in quantum mechanics [1], and after development, has been widely applied in photonics [2,3], plasmonics [4–6], and acoustics [7]. Due to its suppression of radiative loss, the BIC mechanism has been frequently employed to achieve high-quality-factor (high-Q) resonances and played a significant role in research fields of laser generation [8], nonlinear harmonic enhancement [9], highly sensitive sensing [10], and strong photon-exciton coupling [11]. In a broader physical context, by controlling the transition from perfect BICs to quasi-BICs, one can artificially select the coupling state between the resonance and incident light. This approach establishes a versatile platform for systematically investigating light–matter interactions across under-coupled, critical-coupled, and over-coupled regimes [12].

Chiral structures have garnered significant attention because of their notable ability to manipulate photon spin [13,14]. Currently, chiral metasurfaces are primarily categorized into intrinsic and extrinsic types. Intrinsic chirality arises when an object cannot be superimposed onto its mirror image. This fundamental principle has inspired various designs for chiral metasurfaces, including golden helices [15,16], multilayer twisted structures [17,18], near-field-coupled diatomic structures [19–21], asymmetric double-sided scythe structures [22], and inclined unit cells [23,24]. Research on intrinsic chiral structures primarily aims to generate strong circular dichroism (CD) responses upon normal incidence. In contrast, extrinsic chirality emerges from the interaction between the orientation of a metasurface and the propagation direction of the incident electromagnetic wave. Consequently, oblique illumination can induce chiral responses even in inherently nonchiral metasurfaces. This phenomenon has been demonstrated in structures such as planar split rings [25–27] and anisotropic lattices [28–30].

Chirality engineering based on the BIC mechanism enables high-Q resonances with strong CD. Dielectric metasurfaces achieve chirality-maximized quasi-BICs by breaking both in-plane and out-of-plane symmetries [31]. Plasmonic metasurfaces with asymmetric diatomic configurations decouple Q-factor and CD control: the Q-factor is tuned with element height difference, while CD is adjusted by changing relative rotation angle, establishing a new paradigm for sharp chiral responses [20]. Furthermore, oblique incidence exploits momentum asymmetry to modulate radiative loss in quasi-BICs and generate extrinsic chirality via wave vector mismatch, enabling near-perfect absorption with strong CD [27]. However, the strongest responses are typically limited to normal incidence or small-angle oblique incidence (≤60°), limiting manipulation under highly oblique incidence.

In this work, we propose a plasmonic metasurface with cross-shaped metal-insulator-metal (MIM) unit cells to produce strong extrinsic chiral quasi-BICs for large-angle oblique incidence. Specifically, the deep-subwavelength cross-shaped structure can support highly-localized out-of-plane electric dipole (ED) resonances. Simulations show that symmetry breaking, induced by the combined effect of the angle between the cross-arms and the oblique incidence direction, produces a near-perfect absorption resonance at 75° oblique incidence with a high Q-factor (~76) and strong CD (~0.84). By simply tuning the relative azimuth

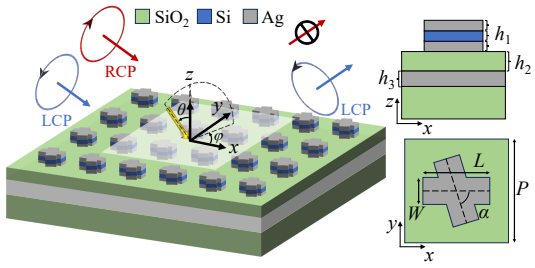

Fig. 1. Schematic of the metal-dielectric hybrid metasurface with strong extrinsic chirality. From bottom to top, the metasurface is composed of an Ag reflective layer, a SiO_2 spacer, and a periodic array of MIM crosses. The designed parameters are as follows: $P = 600\,\text{nm}$, $W = 150\,\text{nm}$, $L = 400\,\text{nm}$, $h_1 = 60\,\text{nm}$, $h_2 = 120\,\text{nm}$, $h_3 = 100\,\text{nm}$, and $\alpha = 70°$.

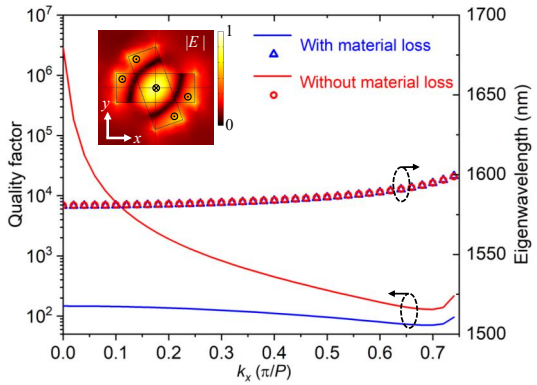

Fig. 2. Eigenmode analysis of the metasurface with (blue) and without (red) material loss. The Q factors and eigenwavelengths are represented by curves and symbols, respectively. The inset shows the eigenmode amplitude profile with the cross and dot symbols denoting $-z$-direction and z-direction polarizations, respectively.

angle between the incident light and the metasurface, the chiral response can be reversed, facilitating dynamic and efficient CD modulation. Our work presents a scheme for the construction and manipulation of strong CD responses applicable to the condition of large-angle oblique incidence. It is helpful to design high-performance systems for on-chip spin selection and chiral biosensing.

In plasmonic systems, minimizing Ohmic loss remains a critical design objective. A significant recent advance has demonstrated that dissipation can be substantially reduced by strategically evolving plasmonic resonances from local to nonlocal regimes [32]. The core idea involves extending the concentrated resonant electric fields into lossless air regions, thereby decreasing their spatial overlap with the high free-electron-density regions responsible for loss. Similarly, for strongly localized plasmonic resonances, high-refractive-index dielectric materials are required to minimize overlap between resonant electric fields and the high-loss region. Therefore, this work employs an MIM structure composed of silver (Ag) and silicon (Si), which simultaneously leverages the strong field confinement properties of metals and the low-loss characteristics of dielectric materials. This configuration supports high-Q localized plasmonic resonances at deep-subwavelength dimensions [33]. The schematic structure of the designed metasurface is illustrated in Fig. 1. An array of MIM crosses with a period P in the x and y directions is placed on a silica (SiO_2) spacer. The three layers of the MIM cross are of equal thickness (h_1). The smaller angle between the two arms of the cross structure is denoted by α. Under the SiO_2 spacer, an Ag layer has enough thickness to prevent light transmission. The incident direction of light is described by the elevation angle θ and the azimuth angle φ. The refractive indices of SiO_2 and Si are modeled using the Sellmeier formula [34] and the data obtained by Li [35] at 293 K, respectively. The complex refractive index of Ag is obtained from the experimental results[36].

We first use the eigenfrequency solver of a finite element modeling software, COMSOL Multiphysics, to analyze the resonant wavelength and the Q-factor of the target mode. The electric field amplitude of the mode is shown in the inset of Fig. 2. The main direction of the electric field is along the z-axis, and the phases of the electric field at the center of the cross and that at the edges of the two arms are opposite. In the calculation, the transverse wave vector component k_x varies from 0 to $0.74\pi/P$, while k_y remains constant at 0. The blue curve and triangles represent Q-factors and eigenwavelengths, respectively, under the original dielectric constant of Ag. The eigenwavelength increases from 1581 to 1599 nm with the growth of k_x from 0 to $0.74\pi/P$. Through wave vector projection calculations, the corresponding elevation angles θ of incidence for the excitation of the eigenmodes range from 0° to 80°. In addition, as k_x increases, the Q-factor initially decreases, reaches a minimum of ~71 around $k_x = 0.7\pi/P$, and then increases.

To reveal the BIC nature of the target resonance, we set the imaginary part of the dielectric constant of Ag to 0 in the simulation. In this case, the Q-factor is only governed by radiative loss. As shown by the red curve in Fig. 2, the Q-factor approaches infinity when $k_x = 0$, and decreases exponentially with the deviation of k_x from the Γ point. Thus, the target mode is a quasi-BIC originating from the symmetry-protected BIC in the momentum space. Furthermore, as indicated by the red circles in Fig. 2, the resonant wavelengths agree with the results obtained when material loss is included. This consistency demonstrates the reliability of the method involving artificial modification of material loss.

Next, we use a full-wave solver to model the reflectance spectra of the metasurface under the excitation of left-circularly polarized (LCP) and right-circularly polarized (RCP) light at different elevation angles. Figure 3(a) shows the reflectance spectra for LCP light at different θ when $\varphi = 0$. It is found that the reflectance dip decreases slowly to the minimum of 0.69 as θ grows from 0° to 40°. Then the resonance weakens with a further increase of θ. However, for RCP incidence, the resonant amplitude exhibits continuous growth alongside increasing θ as indicated in Fig. 3(b). Near-perfect absorption can be obtained at large oblique incident angles. For example, when the incident angle is 75°, the excited resonant amplitude difference for RCP versus LCP achieves 0.83. Moreover, the Q-factor derived from the ratio between the spectrum linewidth and the central wavelength is ~76, which agrees with the result of the eigenmode calculation. Then, we perform multipole decomposition to analyze the components of the resonant mode [37]. Figures 3(c) and 3(d) show the results at 75° incidence for LCP and RCP light, respectively. For both scenarios, the resonant mode exhibits predominant out-of-plane ED characteristics, while the other components, including magnetic dipole (MD), toroidal dipole (TD), electric quadrupole (EQ), and magnetic quadrupole (MQ), are negligible. A notable suppression of

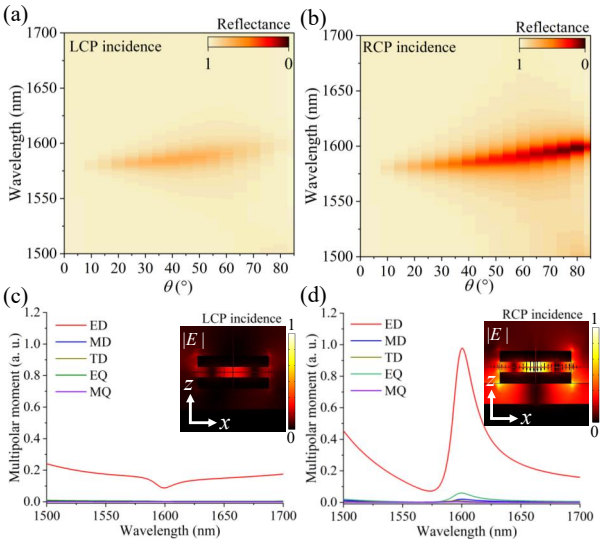

Fig. 3. Reflectance spectra and multipole decomposition results of resonant modes under circularly polarized light illumination on the metasurface. (a), (b) Reflectance spectra under different incident angles θ for LCP and RCP light, respectively. (c), (d) Multipolar decomposition of modes excited at 75° incidence by LCP and RCP light, respectively. The insets in (c) and (d) indicate the electric field profile at the wavelength of 1596 nm in the plane of $y=0$, the black arrows denote the polarization direction.

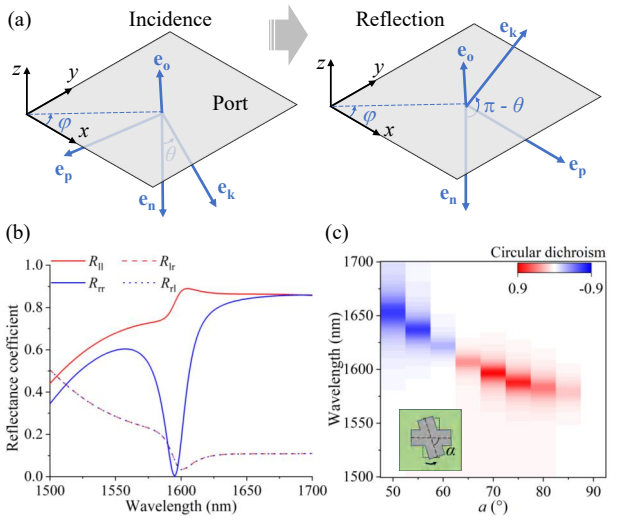

Fig. 4. Simulation results of reflectance coefficients and circular dichroism. (a) Schematic of Cartesian coordinate systems defined by the incident and reflected light propagation direction $\mathbf{e_k}$ and the incident port normal vector $\mathbf{e_n}$, with the port plane parallel to the metasurface. The unit vectors normal to and in the incident plane are defined as $\mathbf{e_o} = \mathbf{e_k} \times \mathbf{e_n}$ and $\mathbf{e_p} = \mathbf{e_o} \times \mathbf{e_k}$, respectively. (b) Reflectance coefficient for LCP and RCP incidence in the case of $\alpha = 70°$, $\theta = 75°$, and $\varphi = 0°$. (c) The circular dichroism spectra of metasurfaces with different α.

excitation amplitude occurs for LCP illumination compared to RCP around 1596 nm. Furthermore, the normalized electric field profile shown in the inset of Fig. 3(d) demonstrates strong field localization at the central region of the MIM cross structure.

To analyze the polarization state transformation between the incident and reflected light, we establish incidence and reflection coordinate systems based on the unit vector normal to the incident port $\mathbf{e_n}$ and the unit vector along the light propagation direction $\mathbf{e_k}$, as schematically shown in Fig. 4(a). The wave vectors of both the incident and reflected light lie within the incident plane. The unit vector orthogonal to the incident plane is defined as $\mathbf{e_o} = \mathbf{e_k} \times \mathbf{e_n}$. Then, another unit vector parallel to the incident plane is defined as $\mathbf{e_p} = \mathbf{e_o} \times \mathbf{e_k}$. Consequently, the modified coordinate system is reoriented to track the propagation direction of incident and reflected light. Here, we define the handedness of circular polarization from the perspective of an observer facing opposite to the wave vector. The unit vectors for the LCP and RCP states are obtained as $(\mathbf{e_p} - i\mathbf{e_o})/\sqrt{2}$ and $(\mathbf{e_p} + i\mathbf{e_o})/\sqrt{2}$, respectively.

Reflectance coefficients for different circular polarizations are defined as below:

$$\begin{pmatrix} I^{\text{out}}_{\text{LCP}} \\ I^{\text{out}}_{\text{RCP}} \end{pmatrix} = \begin{pmatrix} R_{\text{ll}} & R_{\text{rl}} \\ R_{\text{rr}} & R_{\text{lr}} \end{pmatrix} \begin{pmatrix} I^{\text{in}}_{\text{LCP}} \\ I^{\text{in}}_{\text{RCP}} \end{pmatrix}, \tag{1}$$

where I^{in} and I^{out} represent the intensity of incident and reflected light, respectively. The coefficient R_{ll} (R_{rr}) represents the reflectance for preserved co-handed circular polarization, defined as the ratio of the reflected intensity retaining the incident LCP (RCP) state to the incident LCP (RCP) intensity at the metasurface interface. Conversely, R_{rl} (R_{lr}) denotes the cross-handed circular polarization reflectance (or circular polarization conversion efficiency), defined as the ratio of reflected intensity converted to the orthogonal LCP (RCP) state to the incident RCP (LCP) intensity.

Figure 4(b) illustrates the spectra of reflectance coefficients when $\alpha = 70°$, $\theta = 75°$, and $\varphi = 0°$. It is shown that the reflectance coefficients of cross-handed circular polarization R_{rl} and R_{lr} are identical. They fall to the minimum (~0.04) around the wavelength of 1600 nm. However, the reflectance coefficients of co-handed circular polarization R_{ll} and R_{rr} are distinct around the resonant wavelength. It can be seen that R_{rr} approaches 0 at the wavelength of 1596 nm, while R_{ll} remains a large value of 0.83. This substantial reflectance difference leads to strong circular dichroism, which is defined as

$$\text{CD} = \frac{R_{\text{ll}} + R_{\text{rl}} - R_{\text{rr}} - R_{\text{lr}}}{R_{\text{ll}} + R_{\text{rl}} + R_{\text{rr}} + R_{\text{lr}}}. \tag{2}$$

Subsequently, while keeping other conditions constant, we changed the angle α between the two arms of the cross-shaped structure to examine its impact on the CD response. As illustrated in Fig. 4(c), the reflectance spectrum does not have CD responses when $\alpha = 90°$. This is because, when the plane of incidence is parallel to the mirror symmetry axis of the cross-shaped structure, the mutual coupling between the electric and magnetic fields is forbidden. Specifically, in this case, the ED resonance polarizing along the z axis couples exclusively to the incident plane wave possessing electric polarization parallel to $\mathbf{e_p}$, but remains decoupled from the plane wave confined to electric polarization parallel to $\mathbf{e_o}$. As α decreases from 90° to 65°, the value of CD first increases, peaks at approximately 0.84 around 70°, and then decreases. With further reduction of α, CD becomes negative and continues to decrease, reaching −0.69 at $\alpha = 50°$. This effect stems from rotation-induced breaking of the unit cell's in-plane mirror symmetry relative to the incident plane. Consequently, the simultaneous in-plane and out-of-plane

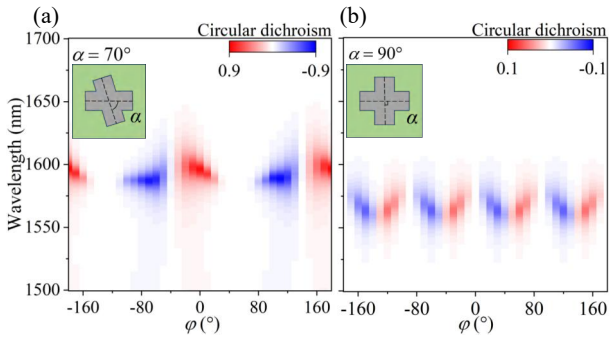

Fig. 5. The CD response of the metasurface as a function of the azimuthal incident angle φ when (a) $\alpha = 70°$ and (b) $\alpha = 90°$. Insets show the top view of the metasurface unit.

mirror symmetry broken induced by geometry and wave vector creates coupling between electric and magnetic components, which leads to a reduction in degeneracy for the LCP and RCP states [20].

Critically, the metasurface enables a wide-range dynamic tuning of CD through azimuthal rotation of the incident plane. Figure 5(a) illustrates the variation of CD with the change of φ when α is 70°. It can be observed that the CD value varies periodically with changes in φ. Due to the C_2 rotational symmetry of the metasurface, the CD variation exhibits a period of 180°. At $\varphi = 0°$, the maximum positive CD is obtained with a value of 0.84. When φ changes to −70° the CD falls to the negative minimum of −0.82. This means that the chirality of the metasurface is entirely flipped. We can notice that the central wavelength of the positive CD peak is ~1596 nm while that of the negative CD valley is ~1587 nm. Such a wavelength deviation is caused by a misalignment between the mirror symmetry axes of the cross-shaped elements and those of the metasurface lattice.

Then we present the circular dichroism spectra for the case of $\alpha = 90°$ in Fig. 5(b). Here, the period of CD variation versus φ is 90° because of the C_4 rotation symmetry of the unit cell. The results show that the absolute value of CD remains lower than 0.07, which indicates that the chirality caused by the lattice orientation is extremely weak. Therefore, the strong CD response is dominantly caused by the asymmetry of the cross-shaped MIM elements. The designed metasurface can be fabricated using established nanofabrication techniques [38]. Detailed processing steps and analysis of fabrication-induced deformation effects are provided in Supplement 1.

In conclusion, we proposed a plasmonic metasurface achieving tunable chiral quasi-BICs under large-angle oblique incidence. The deep-subwavelength cross-shaped element sustains highly localized out-of-plane ED resonances, which enable near-perfect absorption with a high Q-factor of ~76 and strong CD of ~0.84 at 75° incidence. It has been revealed that the observed chirality arises from the simultaneous breaking of in-plane and out-of-plane mirror symmetry, induced by the combined effects of the unit cell's geometry and oblique-incidence wave vectors. Importantly, the chiral response exhibits reversibility through simple tuning of the azimuth incident angle, enabling dynamic and efficient CD modulation in a range from −0.82 to 0.84. Our approach provides a convincing framework for creating and controlling intense CD responses at large oblique angles, advancing high-performance systems for on-chip spin selection and chiral biosensing.

Funding. National Natural Science Foundation of China (12174123, 12374347); Guangzhou Municipal Science and Technology Bureau (SL2024A04J00197).

Disclosures. The authors declare no conflicts of interest.

Data availability. Data underlying the results presented in this paper are not publicly available at this time but may be obtained from the authors upon reasonable request.

Supplemental document. See Supplement 1 for supporting content.

REFERENCES

1. J. von Neuman and E. Wigner, Physikalische Zeitschrift **30**, 467 (1929).
2. D. C. Marinica, A. G. Borisov, and S. V. Shabanov, Phys. Rev. Lett. **100**, 183902 (2008).
3. K. Koshelev, S. Lepeshov, M. Liu, *et al.*, Phys. Rev. Lett. **121**, 193903 (2018).
4. Y. Liang, K. Koshelev, F. Zhang, *et al.*, Nano Lett. **20**, 6351 (2020).
5. Y. Liang, H. Lin, S. Lin, *et al.*, Nano Lett. **21**, 8917 (2021).
6. Z. Wang, Y. Liang, J. Qu, *et al.*, Photonics Res. **11**, 260 (2023).
7. I. Deriy, I. Toftul, M. Petrov, *et al.*, Phys. Rev. Lett. **128**, 084301 (2022).
8. I. Barth, M. Deckart, D. Conteduca, *et al.*, ACS Nano **18**, 12897 (2024).
9. N. Bernhardt, K. Koshelev, S. J. White, *et al.*, Nano Lett. **20**, 5309 (2020).
10. M. Luo, Y. Zhou, X. Zhao, *et al.*, ACS Nano **18**, 6477 (2024).
11. E. Maggiolini, L. Polimeno, F. Todisco, *et al.*, Nat. Mater. **22**, 964 (2023).
12. A. Aigner, A. Tittl, J. Wang, *et al.*, Sci. Adv. **8**, eadd4816 (2022).
13. M. Hentschel, M. Schäferling, X. Duan, *et al.*, Sci. Adv. **3**, e1602735 (2017).
14. J. Mun, M. Kim, Y. Yang, *et al.*, Light: Sci. Appl. **9**, 139 (2020).
15. J. K. Gansel, M. Thiel, M. S. Rill, *et al.*, Science **325**, 1513 (2009).
16. J. K. Gansel, M. Latzel, A. Frölich, *et al.*, Appl. Phys. Lett. **100**, 101109 (2012).
17. J. Zhou, J. Dong, B. Wang, *et al.*, Phys. Rev. B **79**, 121104 (2009).
18. A. Overvig, N. Yu, and A. Alù, Phys. Rev. Lett. **126**, 073001 (2021).
19. Y. Liang, H. Lin, K. Koshelev, *et al.*, Nano Lett. **21**, 1090 (2021).
20. Y. Tang, Y. Liang, J. Yao, *et al.*, Laser Photonics Rev. **17**, 2200597 (2023).
21. M. Choi, A. Alù, and A. Majumdar, Phys. Rev. Lett. **134**, 103801 (2025).
22. T. Shi, Z.-L. Deng, G. Geng, *et al.*, Nat. Commun. **13**, 4111 (2022).
23. X. Zhang, Y. Liu, J. Han, *et al.*, Science **377**, 1215 (2022).
24. Y. Chen, H. Deng, X. Sha, *et al.*, Nature **613**, 474 (2023).
25. E. Plum, X.-X. Liu, V. A. Fedotov, *et al.*, Phys. Rev. Lett. **102**, 113902 (2009).
26. E. Plum, Appl. Phys. Lett. **108**, 241905 (2016).
27. J. Wu, X. Xu, X. Su, *et al.*, Phys. Rev. Appl. **16**, 064018 (2021).
28. V. Yannopapas, Opt. Lett. **34**, 632 (2009).
29. L. Mao, K. Liu, S. Zhang, *et al.*, ACS Photonics **7**, 375 (2020).
30. N. Jiang, J. Shi, C. Shen, *et al.*, Opt. Lett. **50**, 2021 (2025).
31. M. V. Gorkunov, A. A. Antonov, and Y. S. Kivshar, Phys. Rev. Lett. **125**, 093903 (2020).
32. Y. Liang, D. P. Tsai, and Y. Kivshar, Phys. Rev. Lett. **133**, 053801 (2024).
33. Z. Wang, Y. Wang, Z. Cheng, *et al.*, Appl. Phys. Lett. **123**, 121703 (2023).
34. I. H. Malitson, J. Opt. Soc. Am. **55**, 1205 (1965).
35. H. H. Li, J. Phys. Chem. Ref. Data **9**, 561 (1980).
36. P. B. Johnson and R. W. Christy, Phys. Rev. B **6**, 4370 (1972).
37. Y.-W. Huang, W. T. Chen, P. C. Wu, *et al.*, Opt. Express **20**, 1760 (2012).
38. A. Das, C. Mao, S. Cho, *et al.*, Nat. Commun. **9**, 4828 (2018).